Seventh International Conference on Computational Fluid Dynamics (ICCFD7), Big Island, Hawaii, July 9-13, 2012

ICCFD7-3406

Overheating Anomalies during Flight Test due to the Base Bleeding

Dmitry Luchinsky[*], Slava Osipov[*], Halyna Hafiychuck[*],
Ekaterina Ponizhovskaya[*], Vadim Smelyanskiy[*]
Mark Dagostino[**], Francisco Canabal[**], Brandon L. Mobley[**]
Corresponding author: dmitry.g.luchinsky@nasa.gov
* Applied Physics Group, NASA ARC, USA
** EV33/Aerosciences Branch, NASA MSFC, USA.

Abstract: In this paper we present the results of the analytical and numerical studies of the plume interaction with the base flow in the presence of base out-gassing. The physics-based analysis and CFD modeling of the base heating for single solid rocket motor performed in this research addressed the following questions: what are the key factors making base flow so different from that in the Shuttle; why CFD analysis of this problem reveals small plume recirculation; what major factors influence base temperature; and why overheating was initiated at a given time in the flight. To answer these questions topological analysis of the base flow was performed and Korst theory was used to estimate relative contributions of radiation, plume recirculation, and chemically reactive out-gassing to the base heating. It was shown that base bleeding and small base volume are the key factors contributing to the overheating, while plume recirculation is effectively suppressed by asymmetric configuration of the flow formed earlier in the flight. These findings are further verified using CFD simulations that include multi-species gas environment both in the plume and in the base. Solid particles in the exhaust plume (Al_2O_3) and char particles in the base bleeding were also included into the simulations and their relative contributions into the base temperature rise were estimated. The results of simulations are in agreement with the temperature and pressure in the base measured during the test.

Keywords: Base heating, Base Bleeding, Computational Fluid Dynamics, Plume Recirculation.

1 Introduction

The launch vehicle and missiles encounter base heating due to the interaction of free stream and the rocket exhaust. Current research attacks this problem on several directions. Modern experimental techniques [1]-[8] allow for visualization of the base flow with nanosecond resolution [8] including visualization of large coherent turbulent structures [3], [4]. The analysis of small scale experiments and post-flight databases underlies recent progress in the development of the numerical methods [12], [13] suitable for more accurate base flow predictions. The progress in the CFD analysis of the base flow is paralleled with the development of the numerical methods for analysis of the plume radiation. At the same time recent years witnessed renewed interest to the theoretical analysis [16]-[19] of the base flow interaction with rocket plume that continues the line of reasoning developed in the Chapman-Korst theory [20]-[23].

Despite this progress, accurate predictions of the base temperature and heat fluxes during the ascent remain a challenge to computational fluid dynamics. Difficulties stem from the fact that the fundamental

flow multi-physics at the base is not well understood. Often the interplay of the base flow with the plume recirculation, afterburning, chemically active outgassing, and radiation has to be taken into account rendering the problem of the base flow calculations a formidable task.
In particular, recent test flight with single motor first stage design posed a significant challenge in predicting base environment using both semi-empirical approach relying on the shuttle space flight database [23] and CFD solution. Earlier extensive numerical analysis including detached LES simulations revealed unexpectedly that the level of the plume recirculation is substantially below the one required for explanation of the observed overheating. At the same time post flight data analysis indicates significant outgassing at the base that could substantially contribute to the observed increase of the base temperature.
In this paper we present results of the research performed to analyze the root causes of the observed overheating and to facilitate the prediction of the thermal environment for the next generation of the heavy lift vehicle.
The paper is organized as follows. In the next section the problem formulation is presented, the mesh generation, including brief description of the computational methodology, mesh generation and adaptation. The results of the analysis of the base flow with neglected radiation and the base outgassing are presented in Sec. 3. The comparison of the base flow topology observed in numerical simulations with the predictions obtained using recent advances in the Korst theory is given in Sec. 4. The model of the base outgassing and the base bleeding characteristics are discusses in See. 5. The effect of outgassing and afterburning on base environment are discussed in Sec. 6. Finally, a brief summary of the obtained results and discussion of the future work is given in Conclusions.

2 Problem Statement

In a recent test flight of a vertically stacked rocket with single motor first stage a significant overheating of the base environment has been observed. The base temperatures predicted using both CFD analysis [10], [11] and semi-empirical approach [23] significantly underestimate observed base temperature. A deviation of the predicted temperatures from the measured data is found already earlier in the flight. At some points of the flight-trajectory absolute deviations are as high as 65-85% of the predicted values. Similarly, CFD code significantly underestimates observed convective heat transfer coefficient, while semi-empirical methodology provides accurate predictions of the heat transfer coefficient for the second half of the flight. At the same time radiative heat flux predicted using reversed Monte-Carlo code agrees well with the observations in the first half of the flight.
An extensive hybrid RANS/LES simulations performed with substantially improved mesh resolution of the base flow confirmed earlier predictions for the base temperature obtained using Member's baseline model. One of the most important results of the RANS/LES analysis was an observation of relatively small plume recirculation in the base. The predicted levels of the plume recirculation were up to 5 times smaller than levels required for explanation of the observed overheating.
These observations posed significant challenge to the development of the predicting methodologies.
The research presented in this paper addresses the following questions: what are the key factors making base flow in the single motor first stage so different from that in the Shuttle; why CFD analysis of this problem reveals small plume recirculation; what major factors influence base temperature; and why overheating was initiated earlier in the flight.
An important clue to the possible explanation of the measured overheating was an observation of the strong outgassing of the thermal protection system (TPS) is clearly seen on the flight video. Therefore a significant part of the research was devoted to the analysis of the thermal decomposition of the TPS and the changes it introduces in the base flow. We now describe in more details computational methodology and mesh properties of the model.

3 Computational Methodology

Commercial CFX and FLUENT software capable of solving diverse and complex multi-dimensional fluid flow problems was used in this research. Governing equations for the turbulent compressible gas flow were taken in the form

$$\partial_t \rho + \partial_{x_i}\left(\rho U_i\right) = 0 \tag{1}$$

$$\partial_t\left(\rho U_i\right) + \partial_{x_j}\left(\rho U_i U_j\right) = -\partial_{x_i} p' + \partial_{x_j}\left[\mu_{eff}\left(\partial_{x_j} U_i + \partial_{x_i} U_j\right)\right] \tag{2}$$

$$\partial_t\left(\rho h_t\right) - \partial_t p + \partial_{x_j}\left(\rho U_j h_t\right) = \partial_{x_j}\left(\lambda \partial_{x_j} T + \frac{\mu_t}{\mathrm{Pr}_t}\partial_{x_j} h\right) + \partial_{x_j}\left[U_i\left(\tau_{ij} - \rho\overline{u_i u_j}\right)\right] \tag{3}$$

where $\mu_{eff} = \mu + \mu_t$ and $h_t = h + 1/2 U_i U_j + k$. Equation for the pressure has the form

$$p' = p + 2/3\,\rho k + 2/3\,\mu_{eff}\,\partial U_k/\partial x_k .$$

Note that the last term in this equation that involves the divergence of velocity $2/3\,\mu_{eff}\,\partial U_k/\partial x_k$ is neglected in ANSYS CFX.

One of the key features of the base flow that has to be captured in simulations is the flow separation. Accordingly SST model of Menter was chosen as a baseline model following recommendations of the NASA Technical Memorandum [30]. Advanced formulation of the SST model is currently available in the turbulence modeling program lead by Dr. Menter at ANSYS CFX [31]. In this formulation the standard Wilcox model is blended with transformed *k-ε* model resulting in a well-known set of equations

$$\partial_t\left(\rho k\right) + \partial_{x_j}\left(\rho U_j k\right) = \partial_{x_j}\left[\left(\mu + \frac{\mu}{\sigma_{k_3}}\right)\partial_{x_j} k\right] + P_k - \beta'\rho k\omega + P_{kb}, \tag{4}$$

$$\partial_t\left(\rho\omega\right) + \partial_{x_j}\left(\rho U_j \omega\right) = \partial_{x_j}\left[\left(\mu + \frac{\mu}{\sigma_{\omega_3}}\right)\partial_{x_j}\omega\right] + \left(1 - F_1\right)\frac{2\rho}{\sigma_{\omega_3}\omega}\partial_{x_j}\omega\cdot\partial_{x_j} k + \beta_3\rho\omega^2 + P_{\omega b}, \tag{5}$$

with the following set of parameters β'=0.09, α_1=5/9, β_1=0.075, σ_{k1}=2, $\sigma_{\omega 1}$=2, α_2=0.44, β_2=0.0828, σ_{k2}=1, $\sigma_{\omega 2}$=1/0.856. The transport behavior is obtained by a limiter to the formulation of the eddy-viscosity $\mu_t = \rho\alpha_1 k/\max(\alpha_1\omega, SF_2)$ and a standard choice of the blending functions F_1 and F_2.

The CFX wall boundary treatment exploits the robust near-wall formulation of the *k-ω* model and switches automatically from a low-Reynolds number formulation to a scalable wall functions treatment based on grid density. This so-called scalable wall function treatment of the SST model gives more accurate results for a wider range of grid densities.

The CFX solver combines the geometric flexibility of finite element methods with the conservation properties of the finite volume by integrating conservation equations over a control volume. The pressure integral terms in the momentum integral equation and the spatial derivative terms in the integral equations are evaluated using the finite-element approach. An element is described with eight neighboring nodes. The method is using upwind differencing to ensure global convergence.

An important feature of the ANSYS solver is the ability of adaptive refinement of the unstructured mesh using more than one solution variable. For example, the adaptation criteria, A_i, for a given mesh edge *i* of length l_i, is of the form

$$A_i = \sum_j \frac{\left|\Delta\phi_{ji}\right|}{N_{\phi_j}\left|\Delta\phi_j\right|}$$

where ϕ_j is the *j*-th adaptation variable $\Delta\phi_j$ is the global range of this variable over all notes, $\Delta\phi_{ji}$ is the variation of the adaptation variable on a given edge, and $N_{\phi j}$ is a scalar for adaptation variable. For more

than one solution variable, the adaptation criteria are calculated for each variable at each edge, and the sum over all adaptation variables is used.

It is essential in the context of the base flow research that ANSYS solvers allow modeling of multi-component flow with arbitrary number of species. A number of options is available in ANSYS for modeling chemical reactions. However, the rate of chemical reactions in the base is limited mainly by the turbulent mixing. Accordingly, eddy dissipation model and eddy dissipation combined with finite-rate chemistry were used to model afterburning of the TPS outgassing in the base.

The solid phase was modeled using Lagrangian tracking of a number of particles through the fluid for both *Al* particles in the plume and char particles in the base flow. For the drag coefficient a limiter is introduced [28] to ensure correct behavior in the inertial regime that has the form

$$C_D = \max\left(\frac{24}{\mathrm{Re}}\left(1+0.15\,\mathrm{Re}^{0.687}\right), 0.44\right).$$

The particles temperature is determined by the convective heat transfer, chemical reactions, and the absorption/emission of radiation at the particle surface

$$m_p c_p \frac{dT_p}{dt} = hA_p\left(T_\infty - T_p\right) - f_k \frac{dm_p}{dt} H_{reac} + \varepsilon_p A_p \sigma_{SB}\left(\theta_R^4 - T_R^4\right). \quad (6)$$

The heat transfer coefficient is found using Ranz and Marshall correlation

$$Nu = \frac{hd_p}{\kappa_\infty} = 2.0 + 0.6\,\mathrm{Re}_d^{1/2}\,\mathrm{Pr}^{1/3}.$$

The oxidation of the char particles in this model is coupled with eddy dissipation calculation for the combustion of the volatile gases in the gas phase.

Overall ANSYS solvers offer a unique combination of capabilities suitable for the analysis of multi-physics phenomena determining the base environment using limited resources.

The analysis of relative contribution of various heat sources to the base temperature was performed in several steps. Initially the computation was performed for the whole computational domain in a number of points along flight trajectory. The chemical species transport with frozen chemistry equations were solved for both air free stream and plume flow. The chemical composition and distribution of the species (including distribution in the boundary layer near nozzle wall) in the plume flow were provided by the standard NASA code for plume flow field and specified downstream of the nozzle throat at a plane cut through the nozzle flow approximately 1 m away from the nozzle exit.

At the next step the computational domain was reduced to the analysis of the plume free stream interaction at the nozzle exit. The Al particles transport coupled by the momentum and heat transfer to the gas plume flow was added to the model.

Analysis of the convergence of the predictions of the pressure, temperature, and the species distribution as a function of mesh size was performed at the next step. The main attention at this step was paid to the resolution the free shear layers separating from the racket aft skirt and from the nozzle edge and the recompression region including recompression shock. It was important at this step to implement the incremental adaptation capabilities of ANSYS CFX known as hierarchical refinement of unstructured mesh.

Once convergence of the base temperature and base pressure predictions was achieved an extensive analysis of the base for structure, base bleeding, and afterburning was performed to explain low levels of plume recirculation and high base temperatures observed in the test flight.

4 Model Development

4.1 Geometry and Grid Generation

Computational domains and a typical grid structure for a model of the vertically stacked rocket with single motor first stage are shown in Figure 1. Initially unstructured grid with size of a few million cells

was generated using CFX for the whole computational domain. The flow field around the rocket was calculated for several points along the flight trajectory. Next, to improve the resolution of the base flow the computational domain was restricted to the region near the nozzle exit where free stream interacts with plume as show in the Figure 1 (right). The inlet boundary conditions were provided by the solution of the problem in the whole computational domain at the previous step. The fully coupled (except radiation) transport equations for the *Al* particles were added to the model at this stage.

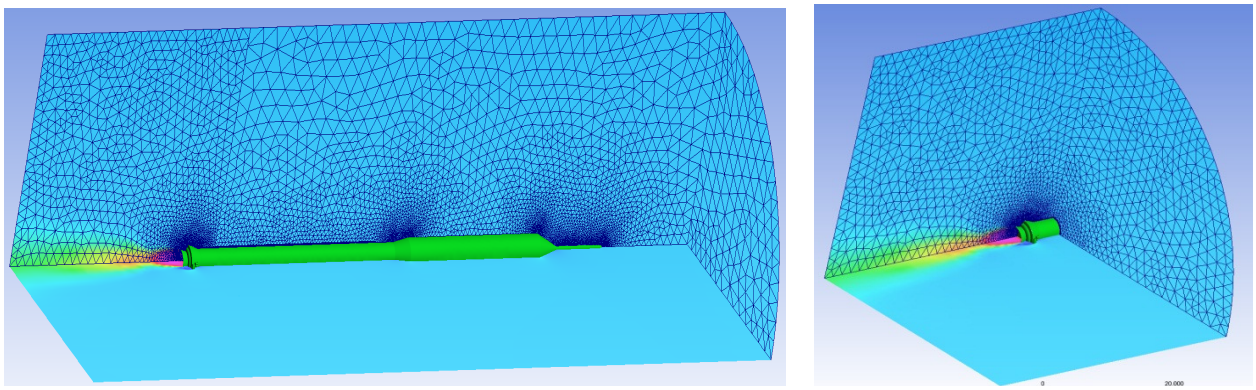

Figure 1: Computational domain for the whole rocket is shown on the left. The computational domain restricted to the flow field around the nozzle is shown on the right.

4.2 Near wall flow resolution

To resolve boundary flow in the near wall regions automatic near-wall treatment for ω-based models was used [28]. According to this approach the boundary layer should be resolved with at least 10 mesh points within the layer for scalable wall functions. The following correlation is used in ANSYS to estimate the width of the boundary layer (δ) in a given computational domain with characteristic length L and Reynolds number Re

$$\delta \propto 0.035 L \mathrm{Re}_L^{-1/7} .$$

The estimated width of the boundary layer for both nozzle flow and base flow was of the order of 0.01m. To satisfy the criteria of the minimum number of nodes for wall function the initial thickness of the mesh layer was taken 5×10^{-4} m and at least 10 layer where placed within boundary layer, while the total number of the boundary layers was 30, as shown in the Figure 2. No attempt was made to resolve heat transfer coefficient at the nozzle wall at this stage of the analysis.

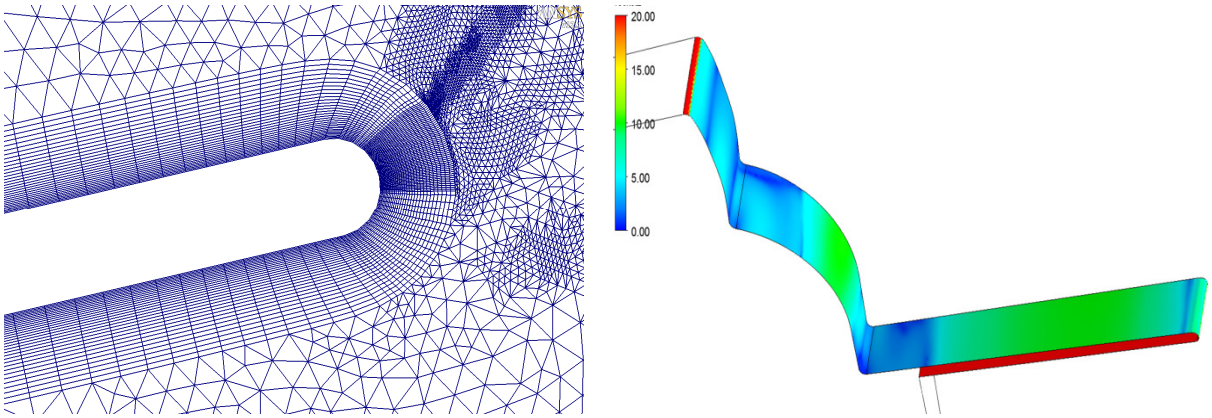

Figure 2: (left) Boundary layers at the nozzle surface. (right) The y+ values at the nozzle surface.

The low-Reynolds number implementation of the model could not be achieved for all the values of used parameters. And automatic near wall treatment that allows for a smooth shift from a low-Reynolds number form to a scalable wall-function formulation was used as default throughout this research.

4.3 Mesh adaptation

In order to resolve free shear layer near the nozzle exit hierarchical refinement of unstructured mesh Mesh adaptation was accomplished in ANSYS CFX. Mesh was selectivity refined in 2 or 3 steps in areas marked for adaptation by the solver depending on specified adaptation criteria. The Mach number was selected as the adaptation variable to guarantee stable and quickly converging solutions. Mesh density was automatically increased in locations where solution variables change rapidly (see Sec. 3 and [28]). Mesh adaptation did not add extra levels to the boundary layers, but rather it added and subtracted nodes within the plane of each layer. Accordingly, mesh adaptation did not change the model's y+ resolution.

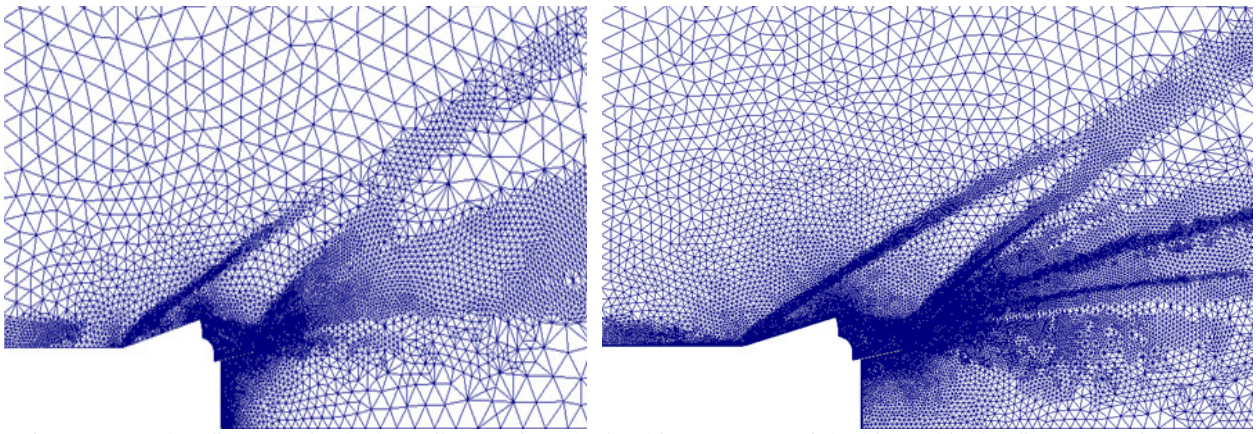

Figure 3: Mesh refinement in the base flow region obtained in two steps of the hierarchical refinement using Mach number variable in adaptation criteria. (left) Mesh before refinement. (right) Mesh after refinement.

The results of the two-step mesh refinement area illustrated in **Figure 3**. The final mesh resolves free shear layers both on the side of the free stream and on the plume side. The size of the mesh depends on the point along the flight trajectory, and in this particular case it was a few million cells.

4.4 Transition to axisymmetric model

The size of the mesh after adaptation for 90° nozzle domain shown in **Figure 1** (right) could be as high as hundred million of cells. To meet the limited computer resources restrictions and in the view of the fact that axial asymmetry of the problem at hand is relatively weak, the computational domain was further reduced to the analysis of a 5° sector. We note that the physics of the base flow in this case is primarily affected by the resolution of the free shear layers. To resolve these layers a very high local mesh density is required near the nozzle edge as shown in the **Figure 2** (left). Note also that using axisymmetric quasi-3D solution in 5° nozzle sector with selective adaptation based on the Mach number variation allows one to reveal important features of the base flow that would otherwise require mesh size of several hundred millions cells to archive similar resolution using nonselective mesh refinement in the 90° nozzle sector.
The results of the analysis of the base flow obtained with this mesh are presented below. In the next section the results of the calculations of the base flow without base bleeding is discussed, the base flow topology is revealed, and the unexpectedly how levels of the plume recirculation observed in the earlier simulations for the vertically stacked rocket with single solid motor are confirmed and explained. The discussion of the base bleeding characteristics and the base bleeding effect on the base temperature will be presented in Sec. 7.

5 Results of the simulations without base bleeding

5.1 Structure of the base flow

Results of the simulations of the free stream interaction with the rocket jet obtained using the model described in the previous section for one point along the flight trajectory are shown in Figure 4 and Figure 5. A high-contrast contour plot of the Mach number distributions reveals clearly the well-known structure

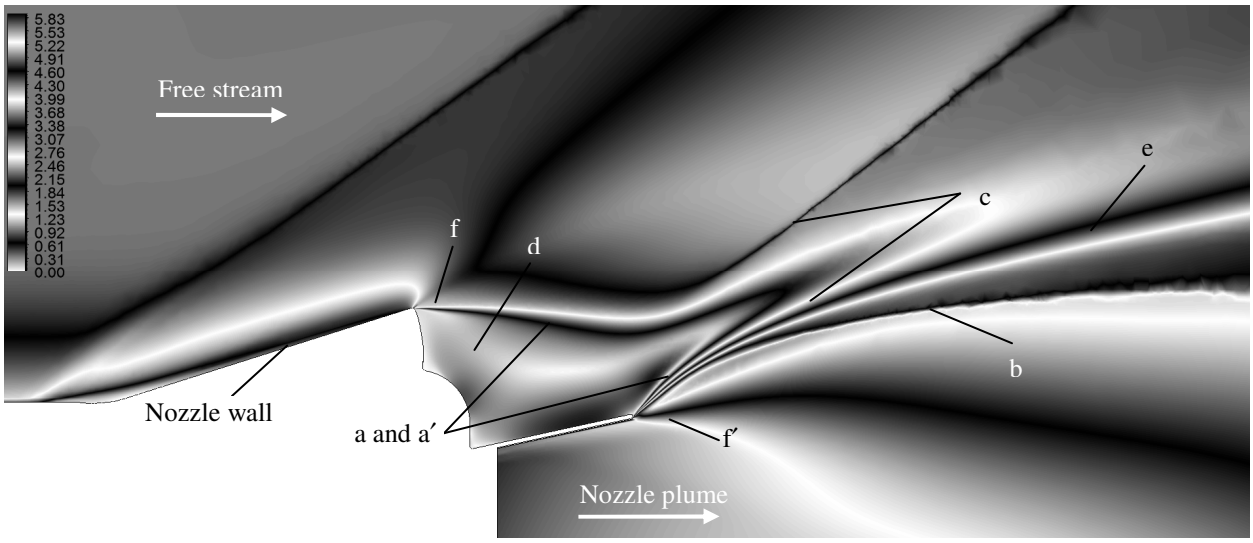

Figure 4: Contour plot of the Mach number: (a and a′) mixing layers; (b) barrel shock of under-expanded jet; (c) recompression shock waves near wake; (d) base flow; (e) plume boundary; (f and f′) expansion fans.

of the flow field corresponding to the free stream interaction with the rocket jet. The two shear layers (a and a′) bounding the base flow (d) on the plume side and the free stream side can be seen in the figure. On passing the rocket skirt the free stream is changing its direction through expansion fan (f) to match the

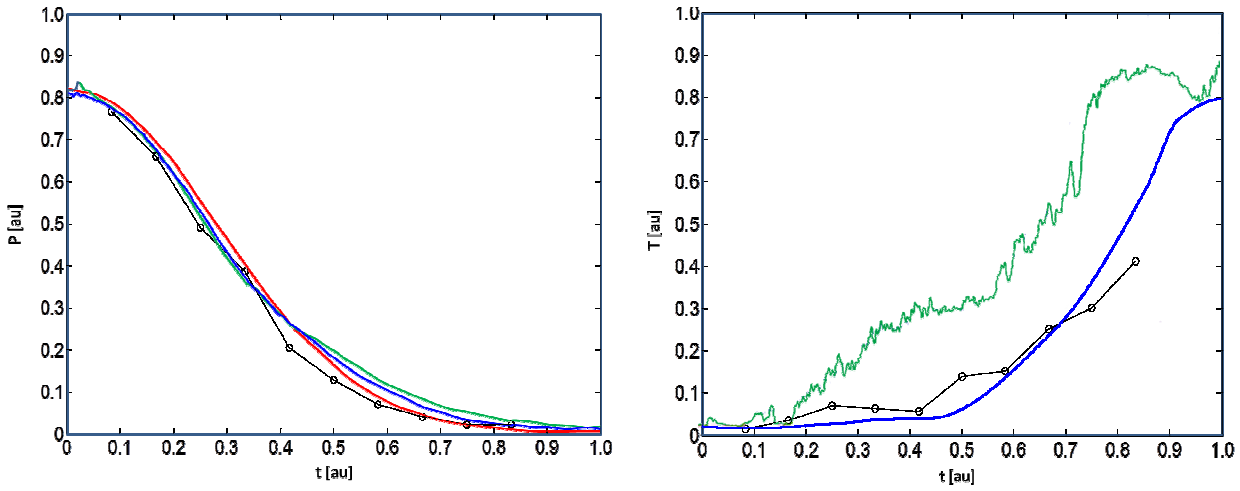

Figure 5 (left) Pressure predictions for various flight trajectories are shown by the open circles in comparison with measured data (blue and green solid lines) and total free stream pressure (red line). (right) Temperature predictions are shown by the open circles in comparison with measured data (green solid lines) and total free stream temperature (blue line).

base pressure. The free stream boundary layer separates from the skirt and forms free shear layer (a) that follows free stream direction. Similarly, on the plume side the under-expanded jet is expanding through

an expansion fan (f′) to match base pressure. The jet boundary layer separates from the nozzle at the nozzle exit and forms free shear layer (a′) that follows the direction of the plume boundary. The two shear layers merge in the recompression zone bounded on both sides by the recompression shocks (c) coupled to the shear layers. As a result, the base flow is trapped between two shear layers.
The results of the calculation of the base pressure for mesh adapted at various points along the flight trajectory are shown in the Figure 5 (left). It can be seen from the figure that the predictions for the base pressure follow very closely the total free stream pressure in good agreement with earlier calculations

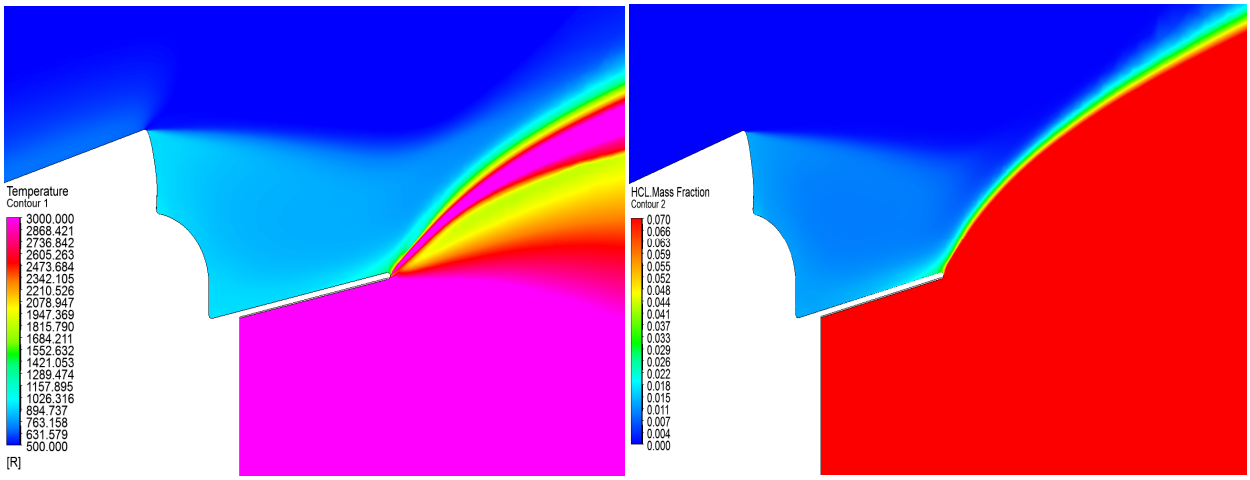

Figure 6: (left) Temperature distribution. (right) HCl mass fraction distribution.

[10], [11], confirmed by the RANS/LES calculations with high mesh density for one specific trajectory point. The pressure predictions are also in good agreement with the measured data for the first part of the trajectory, but underestimate measured pressure later in the flight. Furthermore, calculated pressure fails to predict the crossover of the base pressure with ambient pressure observed during the flight test. Note, that such a crossover usually indicates the mass addition to the base related to the initiation of the plume recirculation [25].
The predicted temperatures are shown in the Figure 5 (right). It can be seen from the figure (see also contour plot of the temperature distribution in the base flow shown in Figure 6 (left)) that predicted temperatures follow closely the total free stream temperature in agreement with earlier calculations [10], [11]. Both earlier calculations and current predictions significantly underestimate observed base temperature already earlier in the flight. At some points of the flight-trajectory absolute deviations are as high as 65-85% of the predicted values.
Earlier research [25]-[27] has shown that the main source of the elevated base temperature is related to the plume recirculation. For example, in the Shuttle [25] or in Titan III [27] plume recirculation is initiated when plume of the two solid rocket motors overlap. In the single motor first stage design plume recirculation may occur only via mass transfer in the mixing layer on the plume side. To explain the observed base overheating plume recirculation at the level approximately 10% of the mass fraction of the base flow is required. However, our calculations show (see Figure 6 (right)) a much smaller level of plume recirculation, which is approximately 1% of the mass fractions the base flow. This result is in agreement with the earlier calculations [10], [11], verified by the RANS/LES calculations for one specific trajectory point.
To understand unexpectedly low levels of plume recirculation in this geometry let us consider base flow topology in more details.

5.2 Topology of the base flow

Topological insight into the key characteristics of the base flow can be obtained using recent advances [16]-[19] of the Korst theory [20]-[24]. According to this theory the flowfield within the shear layers is

divided by two main streamlines $r(r')$ and $s(s')$ for the free stream (plume). The r and r' joint in the end of the wake at stagnation point P_1 in the recompression region as shown in Figure 7 (left). The streamline s terminates in the stagnation point P_2 in the base, while streamline s' propagates downstream along the plume boundary. The importance of the asymmetry of the base flow for the free stream and plume having different total pressure was emphasized in [18], [19], where it was noted that, in general, when two free jet surfaces join, the stronger flow (higher total pressure) is the ejector, and the weaker is the feeder.

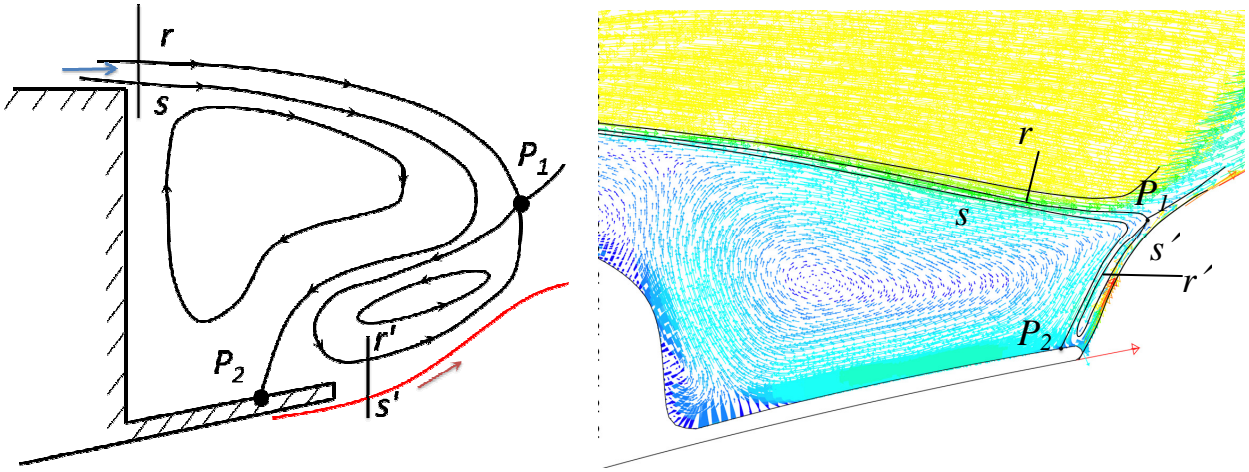

Figure 7: (left) Sketch of the main streamlines separating various regions of the base flow. (right) vector plot of velocity distribution of the base flow colored by the velocity magnitude. Solid lines indicated main streamlines. Solid lines indicated main streamlines separating various regions of the base flow.

This asymmetry is responsible, in particular, for the low levels of the plume recirculation in the current geometry of the base with a single rocket motor. The latter can be understood by identifying location of the key separating streamlines and stagnation points in the vector plot of the base flow velocity as shown in Figure 7 (right). It can be seen from the figure that the pattern of the streamlines r' and s' is degenerate and strongly pressed against the plume boundary because of the very large difference between the total pressures of the free stream and rocket jet. Note that the streamline s impinges the base wall at stagnation point P_2 located at the nozzle exit. We see that the outflow in the corridor s'-r' separates mixing layer on the plume side from the base flow preventing any significant plume recirculation in the base. Therefore the base flow in a given geometry corresponds to the trapped vortex bounded by the streamline s.
Further analysis reveals that transition to the trapped flow occurs earlier in the flight, which correlates well with the initiation of the base overheating observed in the test flight.

To estimate contribution of other physical mechanisms to the base heating let us briefly recall the mixing properties of the shear layers boundary the base flow. The equations for the turbulent shear layer have the form

$$\begin{cases} \left(\overline{\rho u}\right)_{,x} + \left(\overline{\rho \mathrm{v}}\right)_{,y} = 0, \\ \overline{\rho u}\,\overline{u}_{,x} + \overline{\rho \mathrm{v}}\,\overline{u}_{,y} = -p_{e,x} + \left(\left(\mu + \mu_t\right)\overline{u}_{,y}\right)_{,y}, \\ \overline{\rho u}\,\overline{h}_{,x} + \overline{\rho \mathrm{v}}\,\overline{h}_{,y} = \overline{u} p_{e,x} \mathrm{v} + \left(\left(\kappa + \kappa_t\right)\overline{T}_{,y}\right)_{,y} + \left(\mu + \mu_t\right)\left(\overline{u}_{,y}\right)^2. \end{cases}$$

By solving the momentum equation in the incompressible approximation for free mixing layer using Korst theory [18]-[24] one obtains

$$\phi \equiv \frac{u}{u_e} = \frac{1 + erf\left(\eta\right)}{2} = \frac{1}{2} + \frac{1}{\sqrt{\pi}} \int_0^{\eta} e^{-\beta^2} d\beta; \qquad \eta = \sigma \frac{\overline{y}}{\overline{x}},$$

where the compressibility corrections are introduced through the experimentally verified correlations [24], [24]

$$\sigma = 12 + 2.758 M_a .$$

Temperature and pressure distributions can be obtained from Crocco's integral of the boundary-layer equations

$$\frac{T_0}{T_{0a}} = (1-\phi)\frac{T_b}{T_{0a}} + \phi; \qquad \frac{\rho}{\rho_e} = \frac{1 - Cr_e^2}{1 - \phi^2 Cr_e^2}.$$

Once temperature and velocity profiles are established the mass and heat in- and outflows can be determined by integration across streamlines in the mixing layer. For example

$$\dot{m}_{air}^{(in)} = 2\pi R(x)\int_s^r \rho u dy; \qquad \dot{m}_{air}^{(out)} = 2\pi R(x)\int_{r'}^{s'} \rho u dy.$$

Notice, however, that in the first approximation the flow in the corridor between streamlines *s*-*r*, *s*-*r´*, and *s´*-*r´* does not enter the region of the dead air corresponding to the trapped vortex in the base.

It is clear that in the first approximation of the Korst theory there is no ventilation of the air trapped in the base of a single motor rocket. Accordingly, the base temperature is prompt to significant deviations from the total free stream temperature due to various secondary sources of heat. For the air trapped in the base with mass M_p and heat capacity c_p the energy conservation equation reads

$$c_p M_b \frac{dT}{dt} = Q_{bb} + Q_r + Q_{ch} - Q_{loss} + \kappa \left.\frac{\partial T}{\partial x}\right|_s , \tag{7}$$

where the following contributions are taken into account: Q_{bb} is the heat flux due to the base outgassing and chemical reactions, Q_r is the heat flux due to the radiation, Q_{ch} is the heat flux due to the char flux and afterburning. The losses term Q_{loss} is introduced to take into account mass deposition from the base into the mixing layer. The existence of much deposition is clear from the fact that. The term $\kappa \partial T/\partial x|_s$ is the heat flux due to heat conduction at the boundary of the trapped vortex. The last term is automatically included into the base flow calculations described above.

Note that substantial amount of the outgassing was visually detected in the base during the flight test. Therefore in what follows the model is extended to include contributions of the outgassing Q_{ch} and char burning Q_{bb} into the base temperature calculations.

6 Ablation of thermo-protection system

To estimate the mass and heat fluxes in the base due to the base bleeding a model of decomposition of the thermal protection system was developed. The TPS typically consists of Polyurethane (PU) foam, catalysts, blowing agents, surfactants, and flame retardants. In extreme heating environments caused by the plume radiation and heat convection the TPS ablates producing hot gas and smog [32]-[35]. The PU decomposition is a complex process that includes three main steps. First, *endothermal* pyrolysis and internal oxidation of the PU occurs. The energy absorbed during this process is H_p. The products of this reaction are thermo-char with density ρ_{Tc}, gas and oil droplets (yellow smoke) with total density ρ_{gp}. At the second stage, pyrolysis and oxidation of the thermo-char takes place. This reaction is *exothermal* with heat release H_{cT}. The products are α-char (carbon) with density ρ_{ac}, gas and black smoke with total density ρ_{gac}. Finally, combustion and oblation of the porous and friable α-char (carbon) layer formed at the previous step takes place at the TPS surface. This reaction is *exothermal* with heat release H_{ac} [37]. The decomposition products influence essentially the base heating. Using earlier results [33][36] the complex process of PU decomposition, formation of the thermo-char and α-char layer [37] can be reduced to the analysis of the following equations

$$\frac{\partial \rho_p}{\partial t} = -\rho_p R_p(T), \quad R_p(T) = A_p \left(\frac{\rho_p}{\rho_{p0}}\right)^n \exp\left(-\frac{\Delta_p}{T}\right),$$

$$\frac{\partial \rho_{Tc}}{\partial t} = \alpha_{Tc}\rho_p R_p(T) - \rho_{Tc} R_{Tc}(T), \quad R_{cT}(T) = A_{cT}\left(\frac{\rho_{cT}}{\rho_{c0}}\right)^n \exp\left(-\frac{\Delta_{cT}}{T}\right), \tag{8}$$

$$\frac{\partial \rho_{ac}}{\partial t} = \beta_{ac}\rho_{Tc} R_{Tc}(T).$$

Here R_i , A_i and Δ_i are rates, coefficients, and activation energies of the corresponding reactions. Coefficients α_{Tc}, β_{ac} show the fractions of solid thermo-char and α-char that are generated as a result of the pyrolysis of PU and thermo-char; $(1-\alpha_{Tc}), (1-\beta_{ac})$ are the fractions of the gas (see Eqs. (12)-(14)).

The surface α-char layer has a porous structure and can oxidize (burn) in the atmosphere under a large enough heat flow [37], [39]. The rate of the surface processes and flux of the released gas are controlled by density of oxygen ρ_{Ox} near the surface and can be presented as [37]:

$$R_{s,ac,i} = K_{si}\exp(-E/T_s)\, p_{Ox}(t), \quad j_i = \alpha_{ef} R_{s,ac,i}, \quad i = O_2, C, CO, CO_2 \tag{9}$$

where $p_{Ox}(t)$ is the local partial pressure of oxygen at the surface. Here the surface oxidation was described by the following brutto-reaction [37]

$$2\left(\frac{\eta+1}{\eta+2}\right)C + O_2 \Rightarrow \left(\frac{2\eta}{\eta+2}\right)CO + \left(\frac{2}{\eta+2}\right)CO_2, \eta = 70\exp(-3070/TK),$$

$$K_{s,ac} = 2K_s \cdot \left(\frac{\eta+1}{\eta+2}\right)12\times10^{-3} = 3048\left(\frac{\eta+1}{\eta+2}\right), Ks = 1.27\times10^5 \tfrac{mol}{m^2 atm\sec}, \tag{10}$$

$$K_{s,CO} = 2K_s \cdot \left(\frac{2\eta}{\eta+2}\right)28\times10^{-3} = \frac{7112\eta}{\eta+2}, \; K_{s,CO_2} = K_s\left(\frac{2}{\eta+2}\right)44\times10^{-3} = \frac{11176}{\eta+2},$$

$$K_{s,O2} = K_s \cdot 32\times10^{-3} = 4064 \tfrac{kg}{m^2 atm\sec}, \quad E = 1.794\times10^5 \tfrac{J}{mol} = 21588K$$

As a result of the PU pyrolysis a solid pore structure. The gas generated inside the pore structure is released due to pressure gradient at the surface. The decomposition process is very slow and the estimations show that the pressure drop is very small. In other words the gas pressure in the pores is close to the atmospheric pressure. As p_{atm}<*1atm* and $T > T_{atm}$ the gas density $\rho_g \le 1kg/m^3$. Taking into account the fact that density and thermal conductivity of the gas are much smaller than for the solids we can neglect the gas contribution to heat balance that can be written as:

$$\frac{\partial}{\partial t}\left(C_p\rho_p + C_{cT}\rho_{cT} + C_{ac}\rho_{ac}\right)T = \nabla\left[(k_p\frac{\rho_p}{\rho} + k_{cT}\frac{\rho_{cT}}{\rho} + k_{ac}\frac{\rho_{ac}}{\rho})\nabla T\right] + H_p\rho_p R_p + H_{cT}\rho_{cT}R_{cT}, \tag{11}$$

Mass and heat fluxes are determined for the multicomponent outgassing and smog are given by the following expressions

$$j_{gp}(t) = \left(1-\alpha_p\right)\int_{r_s}^{\infty} dr\rho_p(r,t)R_p(T(r,t)), \;\; Q_{gp}(t) = \left(1-\alpha_p\right)\int_{r_s}^{\infty} drC_pT(r,t)\rho_p(r,t)R_p(T), \tag{12}$$

$$j_{gcT}(t) = \left(1-\beta_{cT}\right)\int_{r_s}^{\infty} dr\rho_{cT}(r,t)R_{cT}(T(r,t)), Q_{gcT}(t) = \left(1-\beta_{cT}\right)\int_{r_s}^{\infty} drC_{cT}T(r,t)\rho_{cT}(r,t)R_{cT}(T), \tag{13}$$

$$j_{CO} = R_{s,CO}, K_{s,CO} = \frac{7112\eta}{\eta+2}, Q_{CO} = j_{CO}C_{CO}T_s; \quad j_{CO2} = R_{s,CO2}, K_{s,CO2} = \frac{11176}{\eta+2}, Q_{CO2} = j_{CO2}C_{CO2}T_s, \tag{14}$$

where r_s is the coordinate of moving surface of the burned α-char layer. The velocity of surface motion and mass flow of burned α-char are given by

$$j_{ac} = \rho_{ac,f} v_{ac} = \alpha_{ef} R_{s,ac}, \; v_{ac}(t) = \frac{\alpha_{ef} R_{s,ac}(T_s(t))}{\rho_{ac,f}}. \tag{15}$$

Initial and boundary conditions:

$$T(x,0) = T_0, \; \rho_p(x,0) = \rho_{PU}, \; \rho_{cT}(x,0) = 0, \; \rho_{ac}(x,0) = 0, \; j_{gi}(0) = 0 \tag{16}$$

$$-(k_p \frac{\rho_p}{\rho} + k_{cT} \frac{\rho_{cT}}{\rho} + k_{ac} \frac{\rho_{ac}}{\rho}) \nabla T_s = Q_R + Q_C + H_{ac} R_{s,ac}(T_s) - \varepsilon \sigma T_s^4, \tag{17}$$

$$T_s \equiv T(0), \quad T(\infty) = T_0, \; r_s = \int_0^t v_{ac}(t) dt.$$

Typical values of the parameters used in the calculation are the following. PU parameters: ρ_p=*(23 ÷ 30)kg/m*^{3}, specific heat C_p= *(1000 ÷ 1700) J/kg/K*, thermal conduction K_p= *(0.05 ÷0. 15) W/m/K* [34], [38], [39]. The parameters of PU pyrolysis: A_{pr}= 10$^{10.1}$/sec, Δ_p=1.77x10^4 K, n=0.25, H_p= - 7.5x10^5 J/kg [36] or A_{pr} = 1.686x10^8/sec, Δ_p=1.62x10^4 K, n=0; H_p= *- (2.93-3.47)x10*^{5} *J/kg* [38]. Parameters of thermal char: ρ_{cT}=*(1÷10)kg/m*^{3}, C_{cT}=*1760 J/kg/K,* K_{cT} = *0.05W/m/K* . The parameters of the thermal char pyrolysis and generation of α-char layer: A_{cT}= *10*$^{8.9}$ */sec, n = - 0.08, E=1.25x10*^{4} *K;* H_{cT}= *10*^{5} *J/kg* (with considering retardant) [36]. Heat of combustion of the α-char layer H_{burn}=9.6×10^{6}J/kg [38]. It follows from the calculations that the α-char density is $\rho_{ac,f}$=$\alpha_p \beta_{ch} \rho_p$ =*12.8 kg/m*^{3} *(*$\alpha_p \beta_{ch}$ *=57%,* ρ_p *= 23kg/m).*

Note that the ablation and combustion of the α-char layer takes place in two different scenarios at low and high altitudes. At low altitudes the combustions dominates and ablation is show. As a result the *α*-char layer is growing at the surface blocking heat conduction deep into the TPS. Therefore, the rate of PU pyrolysis and outgassing is small at low altitudes. An example of the results of calculations at low altitude is shown in the Figure 8. It can be seen from the figure that the front of the thermo-char paralysis propagates into the TPS with the rate $v_{Tc} \approx 0.125$ mm/sec, while the recession rate of the TPS surface remains low $v_s \approx 0.046$ mm/sec.

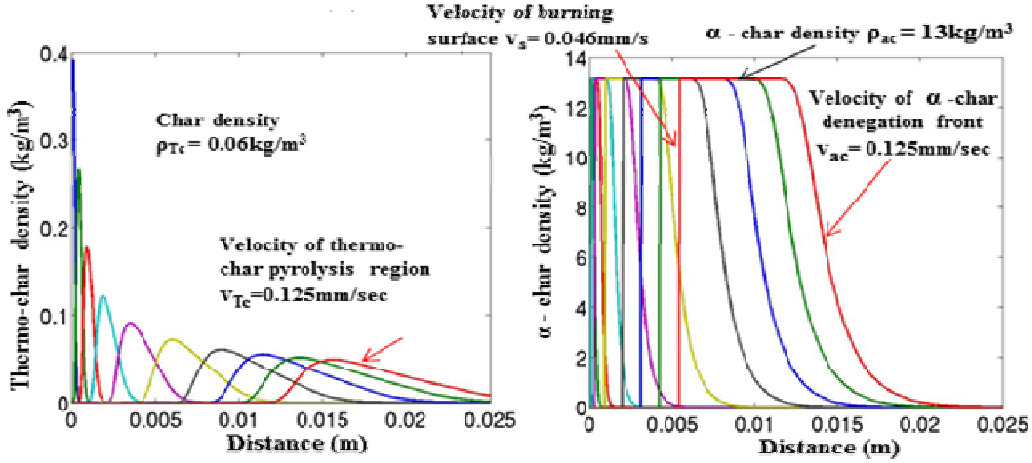

Figure 8: Kinetics of polyurethane foam pyrolysis for low altitudes. Radiation and convection heat flux Q = *4·10*^{4} *W/m*^{2} , oxygen density ρ_{Ox}= *0.2kg/m*^{3} .

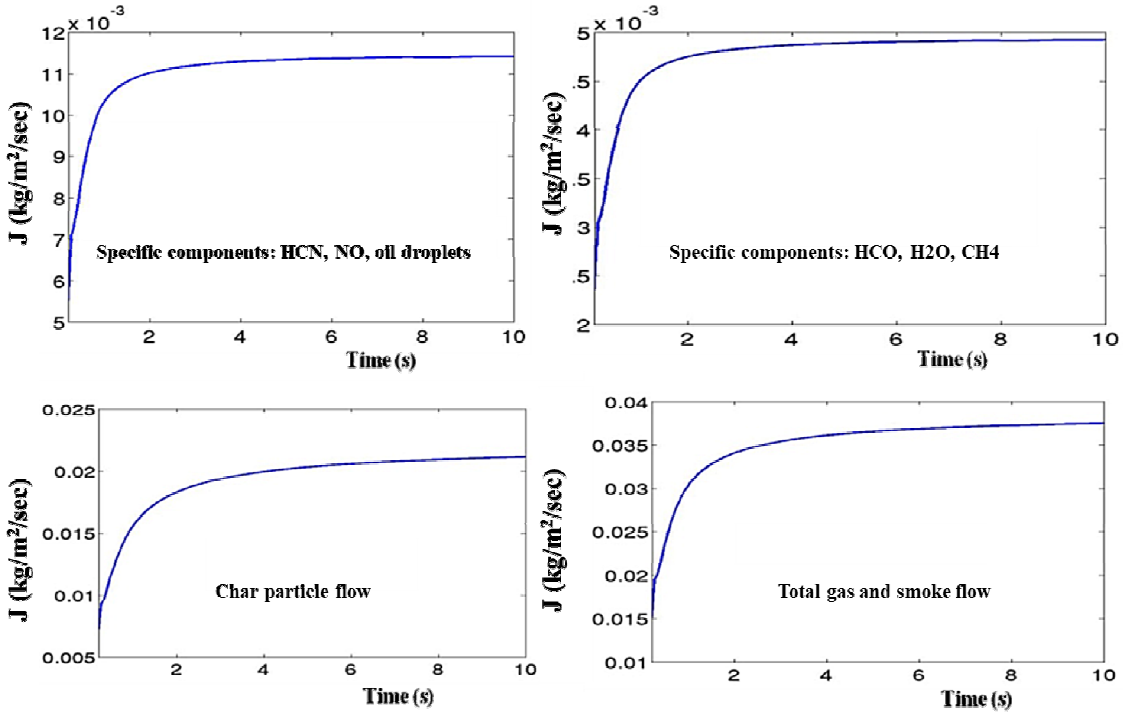

Figure 9: Mass fluxes of gas, smog, oil, and char due to TPS ablation at high altitude. Weak burning and strong convection ablation of α-char layer: was obtained for radiation and convection heat flux $Q = 4 \cdot 10^4$ W/m^2 and oxygen density $\rho_{Ox} < 0.02$kg/m^3.

On the other hand, the higher is the altitude the lower is the concentration of the oxygen and the higher is velocity of the air trapped in the base. As a result, the ablation rate of the α-char layer [40] becomes large, giving rise to the increased flow of char particles with radius 1 to 10 μm and increased recession rate of the TPS surface to the values of the order of 1 mm/sec. This situation is illustrated in the Figure 9 where the mass fluxes of a number of components of the base bleeding are shown for TPS ablation at high altitude.

The results of the calculations of the mass and heat fluxes to the base due to the TPS out-gassing can be used to include multi-component chemically active base bleeding into the CFD model of the base flow introduced in the previous sections. The results of the calculations of the base temperature as a function of the base bleeding parameters are presented and discussed below.

7 Base overheating due to the base bleeding

The analysis of the base environment in the presence of multi-component chemically reactive base bleeding was performed in a number of steps. First, the effect of outgassing with a given mass and heat fluxes was analyzed. Next, the char flow was added to the model. Finally, chemical reactions were included into the calculations.

7.1 TPS outgassing effect on the base environment

It was shown in the previous section that the TPS ablation and outgassing are complex functions of the altitude and base flow. In turn, the base flow depends strongly on the chemical composition, mass and heat fluxes of the TPS bleeding. To establish some of these dependences let us consider first the effect of outgassing on the base environment. Note that the effect of outgassing dominates at low altitudes where the recession rate of the char layer is small while the thermo-char pyrolysis inside the TPS is significant

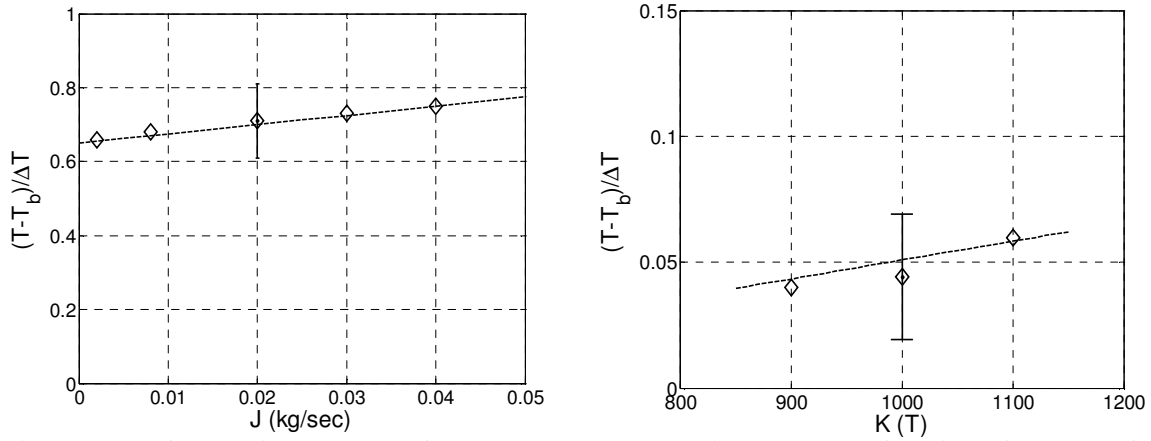

Figure 10: (left) Relative changes of the base temperature (diamonds) as a function of the mass flow rate of the outgassing. (right) Variation of the relative base temperature as a function of the T_{bb}. Straight lines are eye guiding interpolations of the numerical results.

(see Sec. 6). The total gas flow rate and gas temperature estimated at low altitude using chemical kinetic model of section 6 are of the order of J_{bb} = 0.015 kg/sec and T_{bb} = 1200K. These estimations agree well with the experimental results reported in [32]. We now calculate the relative variations of the base temperature as a function of each one of these parameters while all other parameters of the model are kept constant. In particular, the char flow is assumed constant and equal to a small value $J_{char} = 1.5\times10^{-4}$ kg/sec. Examples of the corresponding dependences are shown in the Figure 10. It can be seen from the Figure 10 (left) that base temperature is approximately linear function of J_{bb} in a wide range of variation of base bleeding mass flow rate. The linear dependence of $\tilde{T} = (T_b\text{-}T_{b0})/\Delta T$ on J_{bb} is in agreement with predictions of the simplified model (7) of the temperature of the dead air in the trapped vortex in the base. Indeed, taking $Q_{bb} = J_{bb}\cdot c_p\cdot T_{bb}$, $Q_{ch} \approx 0$, $Q_r = 0$ and assuming that

$$c_p M_b \frac{dT_{b0}}{dt} = -Q_{loss} + \kappa \frac{\partial T_{b0}}{\partial x}\bigg|_s$$

one obtains linear dependence of the $\Delta\tilde{T}$ on J_{bb} in a given time interval Δt. Similarly, the variation of the relative base temperature on the temperature of outgassing T_{bb} is expected to be close to linear. This linearity is confirmed by the calculations of the $\tilde{T}$ as a function of T_{bb} shown in the Figure 10 (right). Note, however, that the relative error of these calculations is much larger than in the calculations of the dependence of $\tilde{T}$ on J_{bb}, because relative changes of the T_{bb} are much smaller as compared to the changes of J_{bb}. Note also that we have assumed above that T_{b0} is independent of the Q_{bb}. This assumption is valid only for relatively small values of the Q_{bb}. In general, the increase of the base temperature is expected to be a saturating function of J_{bb} and T_{bb} as will be discussed in details elsewhere.

7.2 Char flow

The effect of char flow on the base environment is even more complicated. On one hand, the heat exchange between the char particles and the environment is determined by a number of processes including the convective heat transfer, chemical reactions, and the absorption/emission of radiation at the particle surface. On the other hand, particles effectively block and absorb plume radiation, and may effectively escape from the base. In addition, the non-trivial characteristics of the particles behavior depend strongly on their radius.

Consider, for example the rate of reaction at the particle surface given [28]

$$\bar{\mathcal{R}}_j = A_p \eta Y_j \mathcal{R}_j$$

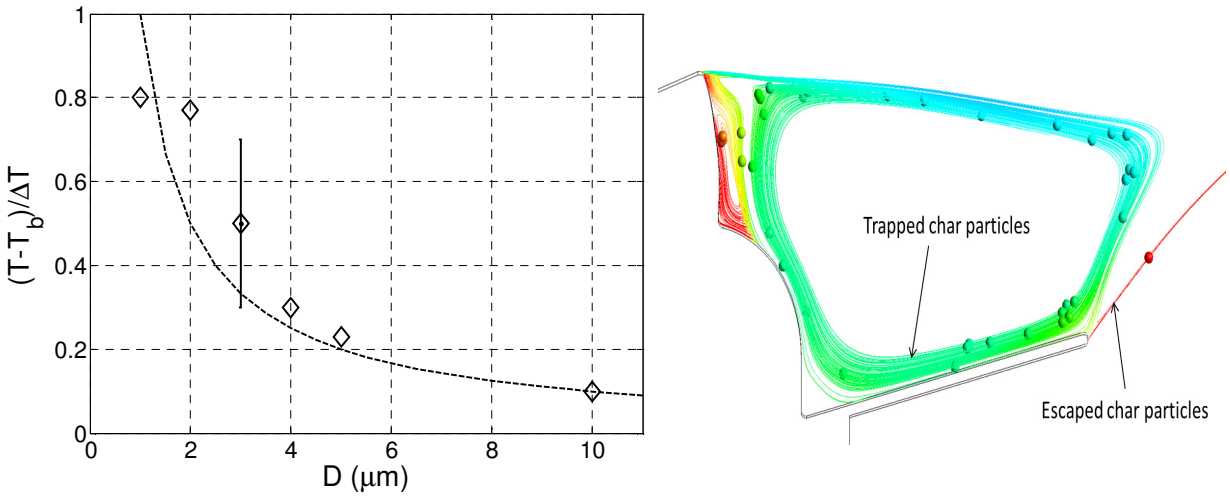

Figure 11: (left) Variation of the relative base temperature as a function of the particle diameter D. Solid line is an eye guiding interpolation of the numerical results by function $\propto 1/D$. (right) Traces of the char particles colored by the temperature showing particles that escape the base flow.

Where $\bar{\mathcal{R}}_j$ is the rate of the particle surface depletion; A_p is particle surface area; Y_j is mass fraction of surface species j; η is effectiveness factor; $\mathcal{R}_j$ is the rate of particle surface species reaction per unit area

$$\mathcal{R}_j = \mathcal{R}_{kin}\left(p_n - \frac{\mathcal{R}_j}{D_0}\right)^N$$

where N = apparent order of reaction:

$$\mathcal{R}_{kin} = AT_p^{\beta} e^{-\left(E/RT_p\right)}.$$

It is clear that the rate of the surface reaction for the alpha-char is directly proportional to the total surface of the alpha particles**.** For constant mass flux $J_{ch} = N4\pi/3 \cdot R^3 \cdot \rho$ and reaction surface of the char particle $A_p = 4\pi R^2$ the total reaction surface $S = N \cdot A_p = 3J_{ch}/R\rho$ and therefore the heat release are inversely proportional to the char radius.

Similarly, radiation and the convective heat transfer are proportional to the particle surface area A_p as shown in the equation (6).

To verify the dependence of the convective heat exchange on the particle radius the variation of the relative base temperature was calculated for constant total char flow rate with different diameter of the char particles, while all other flow parameters were kept constant. The results of these calculations are shown in the Figure 11 (left). It can be seen from the figure that the measured decrease in the base temperature with an increase of the char diameter follows very closely the 1/R type of behavior. We have also verified the dependence of the particles escape rate from the base flow as a function of particle diameter. The results of this analysis demonstrate that the escape rate is larger for the particles of larger diameter. An example of the particles traces is shown in the Figure 11 (right).

It is known from the experiment that the alpha-char particles radius can vary between 0.5 and 50 μ. Therefore, it will be important in the future research to estimate distribution of alpha-char radius experimentally to estimate the effect of alpha-char burning on the base temperature.

The results of the analysis discussed in this section show that the calculated effects of the base bleeding on the base temperature are consistent with theoretical expectations and with the experimental observations of the elevated base temperature during the test flight. In the next section we briefly summarize the effect of the chemical reactions and char burning on the base overheating.

7.3 Chemical reactions and char burning in the base flow

Multiple gas phase reactions occur in the base with the outcome depending on the operating conditions. Several variables seem to affect the gasification process, product composition, and distribution, including temperature, pressure, velocity, and oxygen mass fraction. These parameters are interrelated. The gasification rate is also temperature-dependent. The equilibrium points of the gasification reactions can be shifted by changing the temperature. The first-order rate constant of gasification was found to increase with temperature in accordance with the Arrhenius equation. It was assumed that the mixing of the components in the turbulent base flow was limiting the reaction rates. Accordingly, the eddy dissipation model was used to model chemical reaction in the gas phase with a number of limiters described in [28]. The simplified char combustion process includes three steps of devolatilization, char oxidation and gas-mixture oxidation among which the first two are heterogeneous (multi-phase) and the others are the homogeneous (single-phase) reaction. The eddy dissipation combustion model for homogeneous reactions was used in combination with a finite rate chemistry model for heterogeneous reactions at the particle's surface.

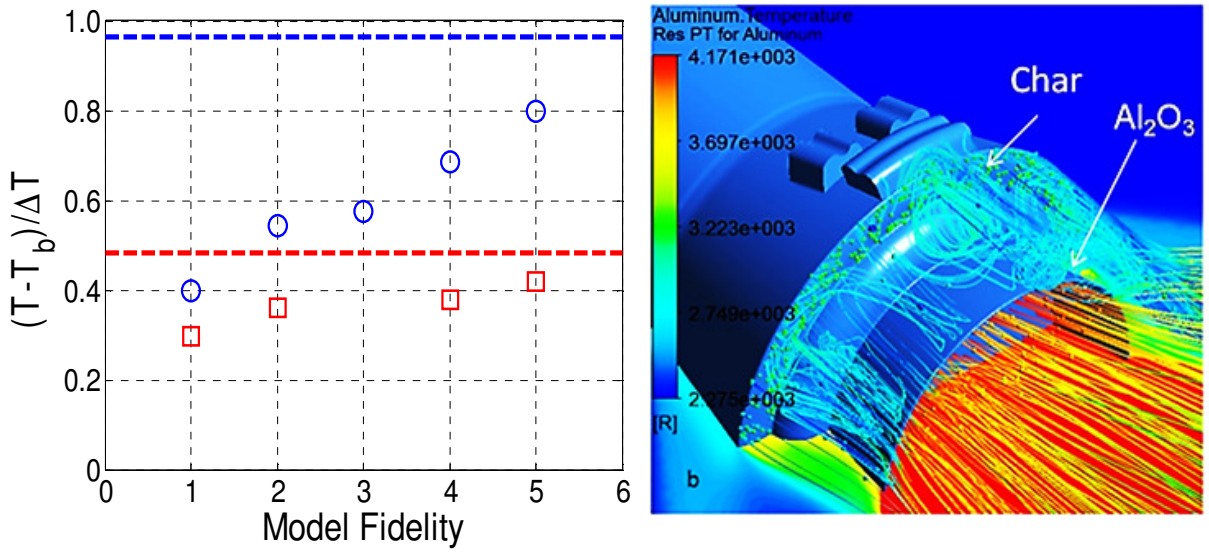

Figure 12: (left) Relative base temperature as a function of the model fidelity for two points on the flight trajectory: 1 - single-phase flow; 2 - Al particles; 3 - radiation; 4 - char burning and chemical reactions (18% of particles with diameter D = 1 μm); 5 - char burning and chemical reactions (64% of 1 μm particles). Dashed lines indicate temperature measured during the flight. (right) Temperature profiles of the free stream plume interaction for multi-phase flow that includes Al particles into multi-component plume flow with frozen chemistry and char particles with multi-component flow with homogeneous and heterogeneous reactions in the base flow.

The results of the calculation of the base temperature that include chemical reactions in the gas phase and char combustion are shown in the Figure 12 (left) for two points on the flight trajectory. Red squares correspond to calculations performed for the point earlier in the flight with different levels of fidelity. In the figure notations 1 corresponds to the calculations performed for multi-component flow with a single gas phase after mesh adaptation. 2 corresponds to the calculations with Al particles included into the plume flow. The last two members 4 and 5 correspond to the multi-component, multi-phase flow with chemical reactions included in the base flow both in gas phase and at the char particles surface (the plume flow assumes frozen chemistry). The difference between 4 and 5 is relative contributions of the char particles with diameter 1 μm. In case 4 particles with diameter $D \approx 1$ μm represent 18% of the total mass flow rate of the char flow. In case 5 they contribute 64% into the total mass flow rate. The dashed lines indicate the base temperature measured for given points of the flight trajectory during the test. It can be

seen from the figure that the temperature calculated for the case of the base bleeding with for homogeneous and heterogeneous chemical reactions is approaching to the base temperature measured during the flight from below.
The remaining gap between measured and calculated temperatures may have multiple origins. One of the contributions to the base temperature neglected so far was the plume radiation. The estimations show that the contribution of the radiation absorption into the elevated base temperature is of the order of 10K. Preliminary calculations of the model of the single-phase base flow that include radiation without chemical reactions are shown in Figure 12 (left) case 3. The results of these calculations are in agreement with the theoretical estimations. Another feature that may contribute to the elevated base temperature that was not included into the current model is an asymmetry of the base flow. Preliminary results of the calculations of the base flow in 90° sector that take into account flow asymmetry are shown in Figure 12 (right) and will be reported elsewhere. The instabilities of the plume base flow interaction during e.g. maneuver during the flight may also result insignificant elevation of the base temperature. Finally, we note that the mass fluxes related to the TPS ablation are known only approximately and further research is required for more accurate predictions. Despite of remaining small discrepancies it can be concluded that the model of the base flow with chemically active base bleeding demonstrates correct trends in the base flow temperature that are consistent with observations and provide an explanation for one of the main sources of the heat flux into the base.

8 Conclusion and Future Work

Theoretical analysis and CFD simulations performed in this research revealed that the base heating anomalies observed in a recent test flight can be attributed to the following factors: small volume of the trapped base air in a single motor first stage configuration; significant base bleeding of hot chemically active components and char trapped in the base; and strong radial asymmetry of the base flow with small region of plume recirculation. An additional important factor that influence the overheating measured during the flight is a strongly non-uniform distribution of the hot flow in the base, which is mainly concentrated along the base walls for both base bleeding and plume recirculation.
It was shown the base flow model with chemically active base bleeding can provide an explanation for one of the main sources of the heat flux into the base. The remaining sources of the heat fluxes that may contribute to significant elevation of the base temperature are plume radiation and transient instabilities of the plume flow. The development of the full 3D model of unsteady base flow that takes into account radiation is under way. The methodology of the base flow analysis developed in this research is currently being transferred, extended, and adopted for base flow in nozzle clusters.

Nomenclature

τ = stress tensor
μ = fluid viscosity
η = effectiveness factor
κ = thermal conductivity
σ =Stephan-Boltzman constant
μ_t = is the turbulent viscosity
μ_{eff} =effective fluid viscosity
$\mathcal{R}_j$ = the rate of particle surface species reaction per unit area
$\bar{\mathcal{R}}_j$ = the rate of the particle surface depletion
A =rates coefficient
A_p = particle surface area

B = non-dimensional pyrolysis gas rate at the surface
B_i =pre-exponential factor for the ith component
C_D = drag coefficient
ch= Char
Cp = particle concentration
c_p =solid material specific heat
c_v = specific heat at constant volume
e = internal energy
H= pyrolysis enthalpy
h= specific enthalpy
H_c total enthalpy of the virgin material
h_{ref} =reference enthalpy
H_v total enthalpy of the charred material
H_w wall enthalpy
J = mass flux of species
k = turbulent kinetic energy
m = mass of the particles
Ma = Mach number
N = apparent order of reaction
n_i = outward unit normal vector at surface i
Nu =Nusselt number
p = the static pressure.
p' = total pressure
Pr = Prandtl number
q = radiative heat flux, W/m^2
Q = the heat flux
R = gas constant
r = Reaction rate
Re = Reynolds number
R_{ex} = radius of nozzle exit
T = temperature
t = time
U_i = the *ith* Cartesian component of the velocity
Δ = activation energies
ε = turbulent dissipation
λ = Conductivity
ρ_1 = fluid density

References

[1] J. L. Herrin, and J. C. Dutton, "Supersonic base flow experiments in the near wake of a cylindrical afterbody", AIAA J., 1994, 32(1), 77–83.

[2] W.J. Bannink, P. G. Baker, and E. M. Houtman, "FESTIP aerothermodynamics: experimental investigation of base flow and exhaust plume interaction", Memorandum M-775, Aerospace Engineering, Delft University of Technology, 1997.

[3] C.J. Bourdon, and J. C. Dutton, "Planar visualizations of large-scale turbulent structures in axisymmetric supersonic separated flows", Phys. Fluids, Vol. 11, No 1,201–213, 1999.

[4] C.J. Bourdon, and J. C.Dutton, "Visualizations and measurements of axisymmetric base flows altered by surface disturbances", AIAA paper 2001-0286, 2001.

[5] C.J. Bourdona and J. C. Dutton, "Visualization of a central bleed jet in an axisymmetric, compressible base flow", Physics Of Fluids, Vol. 15, No 2, 499-510, 2003.
[6] F. Scarano, B. W. van Oudheusden, W. J. Bannink, M. Bsibsi, "Experimental Investigation of Supersonic Base Flow Plume Interaction by Means of Particle Image Velocimetry", Proceedings of the Fifth European Symposium on Aerothermodynamics for Space Vehicles (ESA SP-563). 8-11 November 2004, Cologne, Germany. Editor: D. Danesy., p.601, 2004
[7] P.K. Joel, and J. C. Dutton, "Acetone PLIF imaging of a supersonic axisymmetric base flow with mass bleed", AIAA paper 2004-2650, 2004.
[8] A.L. Kastengren And J.C. Dutton, "Large-structure Topology In A Three-dimensional Supersonic Base Flow", AIAA Journal, Vol. 43, No. 5, May 2005.
[9] A.L. Kastengren, J.C. Dutton, G.S. Elliott, "Large-scale structure visualization and convection velocity in supersonic blunt-base cylinder wakes", Physics of Fluids, 19, 015103, 2007.
[10] S. Tashakkor and F. Canabal, "Loci-CHEM computational fluid dynamics code validation for predicting launch vehicle aerodynamic heating", NASA MSFC Memorandum of Record, 2011.
[11] F. Canabal, J. Mishtawy, and J. West, "Loci-CHEM computational fluid dynamics code validation for predicting plume impingement pressure and heating", NASA MSFC Memorandum of Record, 2008.
[12] M. Mehta, F. Canabal, S. B. Tashakkor, S. D. Smith, "Base Heating Sensitivity Study For A 4-Cluster Rocket Motor Configuration In Supersonic Freestream", NASA Thermal and Fluids Analysis Workshop (TFAWS), Aerothermal Section, 2011
[13] M. Dharavath, P. K.K. Sinha and D. Chakraborty, "Simulation of supersonic base flow: Effect of computational grid and turbulence model", Proceedings of the Institution of Mechanical Engineers, Part G: Journal of Aerospace Engineering 224: 311, 2010
[14] B.E. Pearce, W.H. Wurster, M.C. Flanigan, and K.K. Smolarek, R. Huang "Predictions and Measurements of Radiation Base Heating from a Solid Propellant Rocket Motor Plume", AlAA 91-1431, AlAA 26th Thermophysics Conference, June 24-26, 1991 / Honolulu, Hawaii
[15] M.Y. Kim, M.J. Yu, J.H. Cho "Influence of Particles on Radiative Base Heating from the Rocket Exhaust Plume", Journal of Spacecraft And Rockets, Vol. 45, No. 3, May–June 2008
[16] G. Rubio, A. Matesanz and A. Velazquez, "Prediction of Base Flow / Plume Interaction Including 3-D and Real Gas Effects", AIAA 2000-3171, 36th AIAA/ASME/SAE/ASEE Joint Propulsion Conference and Exhibit, 16-19 July 2000 Huntsville, Alabama, 2000.
[17] M.H. van Raalte and B.W. van Oudheusden, "An Analytical Model to Describe the Reynolds Number Effects in Supersonic Base Flow", AIAA 2001-2785, 31st AIAA Fluid Dynamics Conference & Exhibit, 11-14 June 2001, Anaheim, CA, 2001.
[18] D.-S. Baik, Y.-C. Han, "A Study on Prediction of the Base Pressures for an Axi-Symmetric Body", KSME International Journal Vol. 15, No. 10, 1423-1433. 2001
[19] D.-S. Baik, G.W. Zumwalt, "Analytical Model of the Base Flow Between a Subsonic and Supersonic Flow", J. Of Propulsion And Power, Vol. 18, No 1, 35-43, 2002
[20] R.D. Chapman, "Laminar mixing of a compressible fluid", Technical Note # 1800 (1949).
[21] H. H. Korst, , et al "Compressible Two-Dimensional Jet Mixing at Constant Pressure," ME-TN-392-1, April 1954, Univ. of Illinois, Engineering Experiment Station.
[22] H. H. Khorst, R. H. Page, and M. E. Childs, "A theory for base pressures in transonic and supersonic flow", Contract no. AF 18 (600)-392, Univ. of Illinois, 1955.
[23] R.J. Dixon, J.M. Richardson, and R.H. Page, "Turbulent Base Flow On An Axisymmetric Body With A Single Jet", AlAA Paper NO. 69-650, 1969
[24] J.H. Fox and R.C. Bauer, "Analytical Prediction of the Base Pressure Resulting From Hot, Axisymmetric Jet Interaction in Supersonic Flow", AIAA-81-1898, AlAA Atmospheric Flight Mechanics Conference, August 19-21, 1981 /Albuquerque, New Mexico
[25] T. F. Greenwood and Y. C. Lee, R. L. Bendert, and R. E. Carter, "Space Shuttle Base Heating", J. Spacecraft, vol. 21, no. 4, July-August 1984.

[26] T.L. Kennedy and J.F. Lowry, “An Investigation of Base Heating at a 5.47-percent Scale Model of the Saturn 5-1 Booster at Transonic Mach Numbers”, PWT, ARO Inc., 1961
[27] O.G. Kramer, “Titan III base heating from solid rocket motors exhaust plumes”, AIAA 72-1169
[28] Ansys. User manual, CFX-12 2010, FLUENT-6.3 2008 (Ansys).
[29] F.R. Menter, "Improved Two-Equation k-omega Turbulence Models for Aerodynamic Flows," NASA TM 103975, October 1992.
[30] J.E. Bardina, P.G. Huang, and T.J. Coakley, "Turbulence Modeling Validation, Testing, and Development," NASA TM 110446, April 1997.
[31] F.R. Menter, M. Kuntz, and R. Langtry, "Ten Years of Industrial Experience with the SST Turbulence Model," Turbulence, Heat and Mass Transfer 4, ed: K. Hanjalic, Y. Nagano, and M. Tummers, Begell House, Inc., 2003, pp. 625 - 632.
[32] J.R. Sharp, and A.T. Page, “Ablation Modeling of Ares-I Upper State Thermal Protection System Using Thermal Desktop”, NASA Technical report N 20070037452, 2007.
[33] L.B. Valencia el al, “Analysis of Principal Gas Products During Combustion of Polyether Polyurethane Foam at Different Irradiance Levels, Fire Safety Journal 44, 933, 2009.
[34] L.B. Valencia, “Polyurethane Foam Pyrolysis and Combustion in Cone Calorimeter – Analysis of released heat and gases”, Laboratoire de Combustion et de Détonique, UPR 9028 CNRS, 2007.
[35] G.F. Sykes, Jr., Decomposition Characteristics of a Char-Forming Phenolic Polymer Used for Ablative composites, NASA Technical Note, TN D-3810, 1967.
[36] A. B. Dodd, C. Lautenberger,A.C. Fernandez-Pello, “Numerical Examination of Two-Dimensional Smolder Structure in Polyurethane Foam”, Proceedings of the Combustion Institute, Volume 32; [*www.me.berkeley.edu/cpl/.../dodd_32nd_combustion_symposium.*].
[37] A. K. Sadhukhan, P. Gupta, R. K. Saha, “ Modeling and Experimental Studies on Combustion Characteristics of Porous Coal Char”, [http://onlinelibrary.wiley.com/doi/10.1002/kin.20483/pdf].
[38] K. Prasad, N. Marsh, M. Nyden, T. Ohlemiller, M. Zammarano , “Numerical simulation of fire spread on polyurethane foam slabs”, Fire Research Division, BFRL, NIST Annual Fire Conference, 2009.
[39] M. K. Anderson, R. T. Sleight, J. L. Torero, “Downward smolder of polyurethane foam: ignition signatures”, Fire Safety Journal 35 (2000) 131,147.
[40] B. S. Venkatachari, G. C.Cheng, R. P. Koomullil, “Uncertainty Analysis of Surface Ablation”, 47th AIAA Aerospace Sciences Meeting Including The New Horizons Forum and Aerospace Exposition, Orlando, Florida, 5 - 8 January 2009.
[41] J. Mathew, I. Mahle, and, R. Friedrich, “Effects Of Compressibility And Heat Release On Entrainment Processes In Mixing Layers”, Journal Of Turbulence Vol. 9, No. 14, 2008, 1–12.
[42] R. S. Barlow et al, Combustion and Flame 127:2102-2118 (2001)
[43] J.P. Lamb, W.L. Oberkam, “A Review and Development of Correlations for Base Pressure and Base Heating in Supersonic Flow”, SANDIAREPORT SAND93--0280 • UC—706, (1993)
[44] V. L. Bustamante, T. Rogaume, E. Guillaume, G. Rein, J.L. Torero, “Analysis of principal Gas Products During Combustion of Polyether Polyurethan at Different Irradiance Levels”. 2009